

Spinning nano-carbon grains: Viable origin for anomalous microwave emission

N. Ysard¹, M.-A. Miville-Deschênes², L. Verstraete¹, and A.P. Jones¹

¹ Université Paris-Saclay, CNRS, Institut d'astrophysique spatiale, 91405, Orsay, France

² AIM, CEA, CNRS, Université Paris-Saclay, Université Paris Diderot, Sorbonne Paris Cité, 91191 Gif-sur-Yvette, France
e-mail: nathalie.ysard@universite-paris-saclay.fr

May 12, 2022

ABSTRACT

Context. Excess microwave emission, commonly known as anomalous microwave emission (AME), is now routinely detected in the Milky Way. Although its link with the rotation of interstellar (carbonaceous) nano-grains seems to be relatively well established at cloud scales, large-scale observations show a lack of correlation between the different tracers of nano-carbons and AME, which has led the community to question the viability of this link.

Aims. Using ancillary data and spinning dust models for nano-carbons and nano-silicates, we explore the extent to which the AME that come out of the Galactic Plane might originate with one or another carrier.

Methods. In contrast to previous large-scale studies, our method is not built on comparing the correlations of the different dust tracers with each other, but rather on comparing the poor correlations predicted by the models with observed correlations. This is based on estimates that are as realistic as possible of the gas ionisation state and grain charge as a function of the local radiation field and gas density.

Results. First, nano-carbon dust can explain all the observations for medium properties, in agreement with the latest findings about the separation of cold and warm neutral medium in the diffuse interstellar medium. The dispersion in the observations can be accounted for with little variations in the dust size distribution, abundance, or electric dipole moment. Second, regardless of the properties and abundance of the nano-silicate dust we considered, spinning nano-silicates are excluded as the sole source of the AME. Third, the best agreement with the observations is obtained when the emission of spinning nano-carbons alone is taken into account. However, a marginal participation of nano-silicates in AME production cannot be excluded as long as their abundance does not exceed $Y_{\text{Si}} \sim 1\%$.

Key words. ISM: general - ISM: dust, emission, extinction

1. Introduction

First detected in the 1990s as a dust-correlated excess component above the free-free and synchrotron emissions (e.g. Kogut et al. 1996; Leitch et al. 1997), anomalous microwave emission (AME) has since been observed to be bright in the Milky Way and other galaxies (see the review by Dickinson et al. 2018), with coherent AME structures from scales of degrees down to arcseconds. The prevalent explanation is that the AME carriers are spinning carbonaceous nano-grains emitting through spontaneous emission of purely rotational photons (e.g. Draine & Lazarian 1998a; Ali-Haïmoud et al. 2009; Ysard & Verstraete 2010; Ysard et al. 2010; Silsbee et al. 2011). Other carriers of nanometric size, such as spinning nano-silicates, may also contribute to AME, however (Hoang et al. 2016; Hensley & Draine 2017). Other AME origins were also suggested, such as spinning-grain magnetic dipole emission (Draine & Hensley 2013; Hoang & Lazarian 2016), thermal emission from magnetic dust (Draine & Lazarian 1999) and variations in the sub-millimetre opacity of amorphous solids at low temperature (Jones 2009; Nashimoto et al. 2020). All of these cannot entirely reconcile the low polarisation degree of the 30 GHz AME, which is lower than 1% in the diffuse interstellar medium (see Table 4 in Dickinson et al. 2018, and references therein).

Anomalous microwave emission is a bright component that accounts for about half of the observed intensity at 30 GHz in

the Galactic Plane (Planck Collaboration et al. 2014b, 2016c,b). It is brightest in interstellar regions hosting photon-dominated regions (PDRs; Casassus et al. 2008, 2021; Cepeda-Arroita et al. 2021; Tibbs et al. 2010, among others). These highly irradiated transition regions between HII regions and molecular clouds are known to be sites of strong and rapid evolution of the sub-nanometre hydrocarbon grain populations. Many studies have shown that the abundance of the carbonaceous nano-grains decreases but their minimum size increases from the outer PDRs to the inner molecular clouds. This holds true regardless of the assumed type of carbonaceous nano-grains, that is, PAHs (e.g. Berné et al. 2007; Compiègne et al. 2008; Arab et al. 2012; Pilleri et al. 2012, 2015) or amorphous hydrocarbons a-C(H) (Schirmer et al. 2020), and is taken to be the result of photoprocessing in all cases (see e.g. Murga et al. 2016, 2019). Casassus et al. (2021) showed that this scenario is consistent with AME ATCA observations of the ρ Oph W PDR at an angular resolution of $30''$. They found that the peak frequency of the AME increases from the inner to the outer PDR and that the correlation with mid-IR emission in the Spitzer IRAC $8\mu\text{m}$ filter is tight in the inner PDR, but less so towards the exciting star. Fitting these data with spinning PAHs was possible by adopting an increase in the minimum size deeper into the PDR, in agreement with previous PDR studies based on near- to far-IR observations. As stated by Casassus et al. (2021), at small scales, the AME appears to correlate tightly with the carbonaceous nano-grain mid-IR emis-

sion. This was also shown to be the case for other PDRs (e.g. Casassus et al. 2008; Tibbs et al. 2010, 2011; AMI Consortium: Scaife et al. 2010; Bell et al. 2019; Cepeda-Arroita et al. 2021) and the dark clouds LDN1622 and LDN1780 (Harper et al. 2015; Vidal et al. 2020, respectively). Vidal et al. (2020) found that the observed variations in the 30 GHz emissivity observed in LDN1780 are consistent with spinning PAHs, with size distribution variations from the outer layers to the dense core of the molecular cloud. This agrees with the 3D radiative transfer modelling of IR data performed by Ridderstad et al. (2006).

These small-scale studies clearly illustrate that despite the good agreement between the spinning carbonaceous nano-grain emission model and the observed AME, the correlation between the mid-IR emission and the AME can be rather poor. This is especially true in lines of sight that are dominated by high-density or high-radiation field bright regions, for example, throughout the Galactic Plane. The starting point of our study is to address the challenge to the validity of the rotating carbonaceous nano-grain origin of the AME by Hensley et al. (2016). They performed a full-sky analysis at a 1° angular resolution. Their conclusions were based on the poor correlation of the 30 GHz AME with the observed mid-IR emission and on the way the AME correlates with the dust far-IR to submm radiance. They concluded that other carriers, such as nano-silicates, or other emission mechanisms had to be considered. Using the same AME data as Hensley et al. (2016), we perform a full-sky analysis with the aim of reconciling the small- and large-scale observations. However, our method does not compare the correlations between the different dust tracers, but, in agreement with small-scale studies, compares the poor correlations predicted by the models with observed correlations. In order to be comprehensive, we consider both spinning nano-silicate and nano-carbon dust emission.

The paper is organised as follows. Section 2 describes the data sets and Sect. 3 the dust properties and spinning-dust model. We then discuss the latest observational findings for the density of the neutral gas and its distribution in the diffuse interstellar medium in Sect. 4. Our results are presented in Sect. 5, and we conclude in Sect. 6.

2. Observational data

In addition to maps of the AME, we used data that are characteristic of the thermal emission of grains, both large and small, to carry out our analysis. We also used data characteristic of the radiation field and the column density.

2.1. Planck LFI and HFI foreground products

The Planck observatory¹ carried out a full-sky survey in nine frequency channels between 30 and 857 GHz, that is, ~ 1 cm and $350 \mu\text{m}$. This was subsequently used to estimate the diffuse Galactic emission components: AME and dust thermal emission, and free-free and synchrotron emissions.

For the AME, we used the decomposition made by Planck Collaboration et al. (2016b), which combined the Planck temperature maps in all channels of the Low Frequency Instrument

(LFI: 30, 44 and 70 GHz) and High Frequency Instrument (HFI: 100, 143, 353 and 857 GHz), the 9-year sky maps of the Wilkinson Microwave Anisotropy Probe (WMAP: five channels from 23 to 94 GHz; Bennett et al. 2013), and the Haslam et al. (1982) 408 MHz map. This allowed Planck Collaboration et al. (2016b) to deliver a parametric model of AME at an angular resolution of 1° . The model parameters are available as a healpix map (Górski et al. 2005) with $n_{\text{side}} = 256$ that can be downloaded from the Planck Legacy Archive² (PLA). With these, we computed AME maps at 20, 30, and 40 GHz.

Planck Collaboration et al. (2014a) combined the Planck HFI maps with the IRIS $100 \mu\text{m}$ map (Miville-Deschênes & Lagache 2005). Performing a pixel-by-pixel modified blackbody χ^2 fit, Planck Collaboration et al. (2014a) derived the dust far-IR radiance, $R = \int I_\nu d\nu$, and optical depth at 353 GHz, $\tau_{353\text{GHz}}$. These product maps can be downloaded from the PLA as healpix maps with a 1° angular resolution and $n_{\text{side}} = 256$. The radiance is useful as a good proxy for the radiation field, and the optical depth gives an estimate of the emissivity of large grains that in principle is independent of temperature. Both of these assertions are questionable in the dense molecular regions, however, were large variations in the temperature along the line of sight and variations in the dust grain optical properties are expected (e.g. Planck Collaboration et al. 2014a).

2.2. Thermal dust emission

To characterise the large-grain thermal emission, we used the $100 \mu\text{m}$ map described in Planck Collaboration et al. (2014a). It is a combination of the map of Schlegel et al. (1998) at scales larger than $30'$ and of the IRIS map of Miville-Deschênes & Lagache (2005) at smaller scales. This combination provides the large-scale structure of the maps of Schlegel et al. (1998), which have a higher quality because they are less contaminated by zodiacal light residuals, together with the higher resolution and better calibration of the IRIS map (see Sect. 2.2 in Planck Collaboration et al. 2014a, for details). The IRIS maps are derived from the IRAS data and have an angular resolution of $5'$ and central wavelengths of 12, 25, 60, and $100 \mu\text{m}$ with bandwidths of $\sim 7.0, 11.15, 32.5$, and $31.5 \mu\text{m}$ (Wheelock et al. 1994; Miville-Deschênes & Lagache 2005).

In addition, the nano-grain thermal emission was characterised using the $12 \mu\text{m}$ IRIS map (Miville-Deschênes & Lagache 2005), from which zodiacal residuals were filtered out using a matched filter technique tailored to extracting diffuse emission correlated to the ecliptic reference frame. The technique is described in Appendix A. The 12 and $100 \mu\text{m}$ IRIS maps were smoothed to a full width at half maximum, $\text{FWHM} = 1^\circ$, and projected on a $n_{\text{side}} = 256$ healpix grid.

2.3. Column density map

As stated in Sect. 1, our premise is that AME is produced by the rotation of (sub-)nanometre-sized grains that radiate most of their energy in the near- to mid-IR. It has been known for decades that the dust SED in this spectral range varies strongly depending on the observed interstellar regions (e.g. Laureijs et al. 1991; Abergel et al. 1996; Berné et al. 2007). These variations are commonly interpreted in terms of variations in the size distribution and abundance of nano-grains (see Ridderstad et al. 2006; Vidal et al. 2020; Casassus et al. 2021, for AME related examples). In particular, there is a deficit in the mid-IR

¹ Planck (<http://www.esa.int/Planck>) is a project of the European Space Agency (ESA) with instruments provided by two scientific consortia funded by ESA member states and led by Principal Investigators from France and Italy, telescope reflectors provided through a collaboration between ESA and a scientific consortium led and funded by Denmark, and additional contributions from NASA (USA).

² <http://pla.esac.esa.int/pla/>.

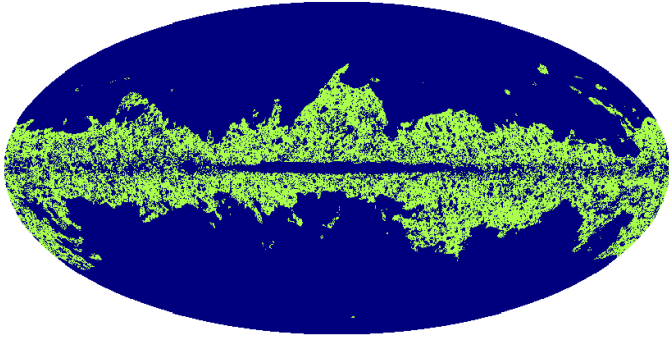


Fig. 1. Mask used to make the analysis. We used the green pixels.

relative to the far-IR emission at atomic diffuse lines of sight compared to lines of sight containing molecular clouds. This can be explained by the disappearance of the small nano-grains together with the growth of the larger grains by grain-grain coagulation (e.g. Bernard et al. 1999; Stepnik et al. 2003; Flagey et al. 2009; Ysard et al. 2013). This disappearance is in agreement with the variations observed in the 2175 Å bump towards molecular clouds (e.g. Mathis & Whiffen 1989; Kim et al. 1994; Campeggio et al. 2007), while the growth of the larger grains can explain the observed increase in selective extinction R_V (e.g. Ormel et al. 2009; Köhler et al. 2015).

Furthermore, regardless of their specifics in terms of composition and initial grain size distribution, all models indicate that the disappearance of the nano-grains occurs and the growth of larger grains starts to occur at still relatively low densities of the order of (a few) 10^3 H/cm³. This has been shown from observations of (i) the thermal emission of grains from the mid- to far-IR (e.g. Ridderstad et al. 2006; Ysard et al. 2013; Saajasto et al. 2021), (ii) the near- to mid-IR scattering known as cloudshine and coreshine (e.g. Lefèvre et al. 2014; Ysard et al. 2016; Juvela et al. 2020), and (iii) the polarisation (e.g. Fanciullo et al. 2017; Vaillancourt et al. 2020). Depending on the dust model details and the gas local properties, the accretion of the (sub-)nanometre-sized grains on larger grains is not expected to take more than a hundred to a few thousand years in the outskirts of molecular clouds (e.g. Stepnik et al. 2003; Köhler et al. 2012; Ysard et al. 2013; Jones et al. 2014). Therefore, when we start from the assumption that nano-grains cause the AME, then the microwave flux must come primarily from the atomic diffuse interstellar medium, and the HI column density should be used when the AME and the 12 μm emission are modelled.

Consequently, the HI column density map we used is that of the HI4PI survey (HI4PI Collaboration et al. 2016). It was constructed by adding all velocity channels between -90 and +90 km s⁻¹ to avoid emission from high-velocity clouds. The native angular resolution of this map is FWHM = 16.2'. It was then convolved with the required complementary Gaussian beam to bring the map to FWHM = 1° before we reprojected to a $n_{\text{side}} = 256$ healpix grid.

2.4. Masks

In the following, we exclude a number of pixels from our analysis. First, as we focused on the neutral diffuse medium, we excluded the Galactic Plane, which contains many molecular re-

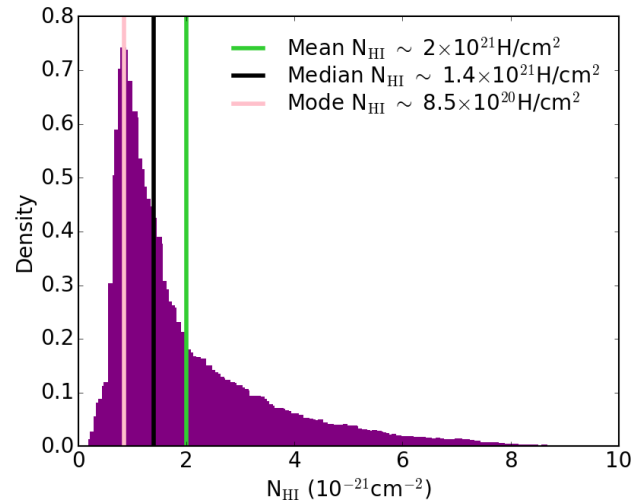


Fig. 2. Histogram of the column density of the pixels we selected for the analysis.

gions as well as very bright HII complexes (e.g. Cygnus X) that are too complicated to be modelled globally. To do this, we used the mask defined by Planck Collaboration et al. (2016a), based on the intensity at 353 GHz, excluding 1% of the sky. We also excluded the point sources detected in the six Planck HFI frequency channels at 100, 143, 217, 353, 545, and 857 GHz and in the Planck LFI 30 GHz channel (Planck Collaboration et al. 2016a). This resulted in an exclusion of ~ 23% of the sky for healpix maps with $n_{\text{side}} = 256$. A third mask was applied to the data to exclude pixels for which the S/N < 3 in the 30 GHz AME map. This led to the rejection of high Galactic latitude pixels for which the AME intensity was very low and covered less than 1% of the sky. According to Planck Collaboration et al. (2016c), the component separation solution in these pixels is dominated by instrumental noise. Finally, we removed the sky area where the S/N < 3 in the 12 μm IRIS map. The uncertainty in these mainly high-latitude areas is dominated by the uncertainty in the subtraction of the zodiacal emission. This amounts to eliminating ~ 63% of the sky. The resulting mask is displayed in Fig. 1. It mainly excludes the Galactic Plane and the highest-latitude regions, that is, about 76% of the sky.

This leads to data with column densities ranging from ~ 10^{20} to 1.4×10^{22} H/cm² (Fig. 2). The mean, median, and mode of the column density distribution are ~ 2×10^{21} , 1.4×10^{21} , and 8.5×10^{20} H/cm², respectively. The standard deviation is ~ 1.5×10^{21} H/cm².

3. Models: Spinning and thermal dust emission

All estimates presented in the following were obtained with the numerical code DustEM³ (Compiègne et al. 2011). DustEM is a versatile numerical tool that is mainly used to calculate the extinction and thermal emission (polarised or unpolarised) of any grain model. A calculation of the spinning dust emission is also implemented. The specificity of this implementation is that it allows the user to process all the parameters involved in the calculation of the excitation and damping of the grain rotation in a consistent way according to their size and composition.

The rate of grain rotation depends on their emission of rovibrational and rotational photons, and on how they interact with

³ Available here: <https://www.ias.u-psud.fr/DUSTEM/>.

the gas. To quantify these interactions, it is necessary to know the charge distribution of the grains and the main parameters describing the state of the gas. These parameters are its temperature T_{gas} , the electron abundance $x_e = n_e/n_H$, the molecular fraction $y = n(\text{H}_2)/n_H$, and the ionisation fraction of the main species $x_H = n(\text{HII})/n_H$, $x_C = n(\text{CII})/n_H$, where $n_H = n(\text{HI}) + n(\text{HII}) + 2n(\text{H}_2)$. The equilibrium charge distribution $f(Z)$ of grains per size and type was computed using the Kimura (2016) model for the photoemission yield and the Wein-gartner & Draine (2001) formalism for the remaining processes⁴. In turn, the parameters describing the gas state were computed using the formalism described in Ysard et al. (2011).

3.1. Dust properties

The dust properties we used are those of The Heterogeneous dust Evolution Model for Interstellar Solids (THEMIS⁵, Jones et al. 2017). It assumes that dust in the diffuse interstellar medium consists of small nano-grains of aromatic-rich carbon (radius $0.4 \leq a \leq 20$ nm) and larger core-mantle grains, for which the cores are composed either of amorphous aliphatic-rich carbon or of a mixture of amorphous silicates with the normative chemical compositions of olivine and pyroxene (with half of the total mass of silicate grains in each type). For all types of grains, the mantles are made of aromatic-rich carbons with a thickness of 20 nm for the carbon cores and 5 nm for the silicate cores. Moreover, iron and sulphur are incorporated into the silicate cores in the form of metallic nano-inclusions of Fe and FeS. They represent 10% of the total core volume, of which 30% is FeS and 70% is pure Fe. This model allows reproducing the emission and extinction curves that are representative of the diffuse medium at high Galactic latitude from the optical to the sub-millimetre (c.f. Jones et al. 2013; Ysard et al. 2015).

To model spinning nano-carbon dust emission, we used the default size distribution of THEMIS, which is a power law $\propto a^{-5}$ with an exponential cut-off and a minimum size of 0.4 nm. We assumed their permanent electric dipole moment to be $\mu \sim m\sqrt{N_{\text{at}}}$, where N_{at} is the number of atoms in the grain and $m = 0.38$ D (see references in Draine & Lazarian 1998b). The THEMIS nano-carbon grains have (Jones 2012a,b,c)

$$N_{\text{at}} = 2500 \left(\frac{a}{1 \text{ nm}} \right) \left(\frac{\rho}{12 - 11X_H} \right), \quad (1)$$

where X_H is the grain hydrogen fraction and ρ is its density, which are equal to 0.023 and 1.6 g/cm³ for the nano-carbons of interest for rotational emission.

THEMIS does not include nano-silicates. To date, the observations have not provided any evidence of their presence in the diffuse medium. However, this lack of detection does not rule them out as a minority constituent, and other dust models include nano-silicates and have placed tentative upper limits on their abundance (e.g. Désert et al. 1986; Li & Draine 2001). In addition to the THEMIS dust components, we followed the studies of Hoang et al. (2016) and Hensley & Draine (2017) and defined a size distribution for nano-silicates and set their electric dipole moment and abundance to model spinning nano-silicate dust emission. To be able to explain AME by the rotation of nano-silicates without contradicting other observations, they cannot contain more than 14% of the available silicon and their dipole moment per atom must be $0.2 \leq m \leq 1$ D, according to

these two studies. To estimate the nano-silicate dipole moments, we assumed that they are a 50%-50% mixture of grains that have the normative compositions of forsterite and enstatite so that we were able to calculate the number of atoms as a function of their size. For the size distribution, both studies assumed log-normal distributions centred on a subnanometric size a_0 and of variable width σ . In contrast to Hoang et al. (2016), Hensley & Draine (2017) took into account the sublimation rates calculated by Guhathakurta & Draine (1989) to set a minimum nano-silicate grain size. They found that when it is illuminated by the average interstellar radiation field, the critical survival size is of 37 atoms, that is, about 0.45 nm. For the models we present below, we define four cases, assuming that $Y_{\text{Si}} = 10\%$ of the total silicon included in dust is locked in nano-silicates, the upper limit derived by Li & Draine (2001), and that $a_0 = a_{\text{min}} = 0.45$ nm as in Hensley & Draine (2017):

- case 1: $m = 0.3$ D and $\sigma = 0.3$;
- case 2: $m = 0.3$ D and $\sigma = 0.1$;
- case 3: $m = 1$ D and $\sigma = 0.3$;
- case 4: $m = 1$ D and $\sigma = 0.1$.

This roughly covers the parameter space defined as acceptable by Hoang et al. (2016) and Hensley & Draine (2017).

3.2. Properties of the local medium

To compare them with observations, model grids were generated for nano-carbons and nano-silicates. When the dust properties are settled, DustEM only requires three inputs: the radiation field, the gas density, and the gas temperature.

We assumed that the interstellar radiation field illuminating the grains has the same spectral distribution as the field of Mathis et al. (1983). Its intensity was then scaled by the G_0 factor with $0.1 \leq G_0 \leq 20$ and $G_0 = 1$ corresponding to the Mathis et al. (1983) standard field intensity in the solar neighbourhood. For the gas, we started from a highly diffuse medium with $n_H = 0.05$ H/cm³ to reach densities that are representative of translucent clouds with $n_H = 1000$ H/cm³. This wide range of parameters should enable us a priori to account for the physical conditions of most lines of sight of the out of Galactic Plane that we considered. The corresponding gas temperatures were computed with CLOUDY (Ferland et al. 1998). The other gas parameters were directly calculated by DustEM (see Ysard et al. 2011, for details).

3.3. Resulting spectral energy distributions

We show two sets of modelling results in Fig. 3. Firstly, the left panel shows the emission spectra of media with $G_0 = 1$ and local gas densities of $n_H = 0.1$ and 30 H/cm³ for spinning nano-carbons (top left) and spinning nano-silicates (bottom left). Secondly, the right panels present the predicted correlations between the mid-IR thermal emission in the IRAS 12 μm filter and the spinning dust emission at 30 GHz. These results highlight the spinning-dust intensity dispersion at 30 GHz as a function of G_0 and of the local gas density n_H . Comparing lines of sight with the same column density that are dominated by low ($n_H \sim 0.1$ H/cm³), moderate ($n_H \sim 30$ H/cm³), or high densities ($n_H \sim 1000$ H/cm³), the latter being typical of translucent clouds, we expect for $G_0 = 1$ spinning-dust 30 GHz intensity variations of about two orders of magnitude for nano-carbons, while for nano-silicates, with $m = 0.3$ and 1 D, the intensity varies by two and six orders of magnitude, respectively.

⁴ Details about the model can be found here: <https://www.ias.u-psud.fr/DUSTEM/userguide.html>.

⁵ Available here: <https://www.ias.u-psud.fr/themis/>.

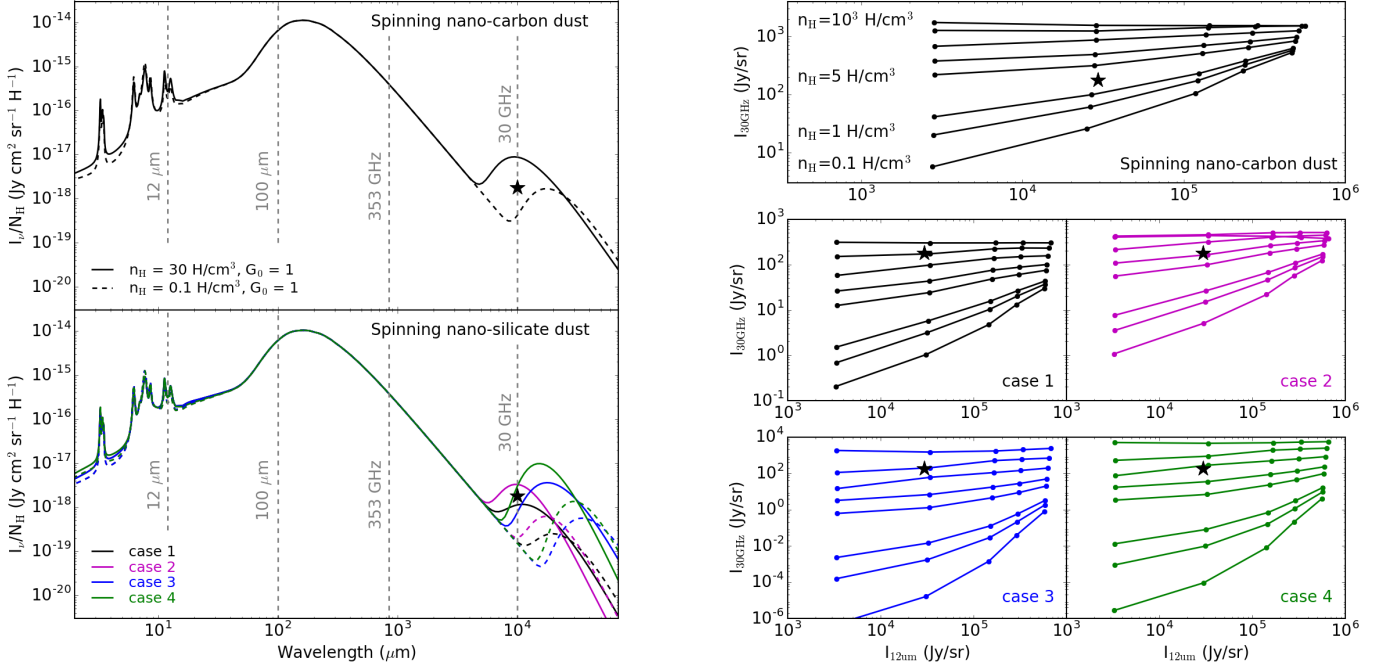


Fig. 3. Thermal and spinning dust modelling results. Left: Dust SEDs for media illuminated by the ISRF with $G_0 = 1$. The dashed and solid lines show media with gas local densities of 30 H/cm^3 and 0.1 H/cm^3 , respectively. The black star shows the average AME emissivity at 30 GHz for the bulk of pixels included in the 50% contour in Fig. 5, to avoid pixels with the highest and lowest densities and radiation fields. The upper panel shows spinning nano-carbon grains, and the bottom panel presents spinning nano-silicates with case 1 in black, case 2 in magenta, case 3 in blue, and case 4 in green; see Sect. 3.1 for details. Right: Spinning nano-dust emission at 30 GHz vs. thermal nano-dust emission at $12 \mu\text{m}$ for $N_{\text{HI}} = 10^{20} \text{ H/cm}^2$. Each panel shows the results obtained for media with densities $n_{\text{H}} = 0.1, 0.5, 1, 5, 10, 30, 100$, and 1000 H/cm^3 from bottom to top. The radiation fields scaled by $G_0 = 0.1, 1, 5, 10$, and 20 are shown from left to right. The upper panel displays spinning nano-carbons. The lower panels show the four cases of spinning nano-silicates described in Sect. 3.1: case 1 in black, case 2 in magenta, case 3 in blue, and case 4 in green. The black star shows the average AME emissivity at 30 GHz vs. the average emissivity at $12 \mu\text{m}$, both scaled to $N_{\text{H}} = 10^{20} \text{ H/cm}^2$.

The spinning nano-carbon models appear to be spread rather evenly about the observational data point, while the spinning nano-silicate models tend to lie below this point. We note that the $12 \mu\text{m}$ intensity remains almost constant for all of the considered models. This implies that the poor correlation of mid-IR emission to 30 GHz AME that is predicted from the spinning nano-carbon models must be even lower in the spinning nano-silicate model. This correlation does not improve when instead of the $12 \mu\text{m}$ thermal emission, we consider the emission at $100 \mu\text{m}$. Therefore, the quality of the 30 GHz versus 12 or $100 \mu\text{m}$ correlation alone cannot be used to exclude any particular carrier. Then, if only the abundance of nano-carbon dust is allowed to vary (for a constant size distribution and constant environment properties), the spinning nano-carbon dust models predict a positive correlation between $\text{AME}_{30\text{GHz}}/N_{\text{HI}}$ and $I_{12\mu\text{m}}/R$, both proportional to the nano-carbon dust abundance. No such correlation is present in the observations (see e.g. Hensley et al. 2016). This lack of correlation is a strong constraint on the models, and we further explore it in Sect. 5. Spinning nano-silicate models predict a weaker correlation because the nano-silicates account for only $\sim 18\%$ of the total emission in the IRAS $12 \mu\text{m}$ band for $G_0 = 1$.

Based on the results presented in Figs. 3 and 4, we make two remarks concerning the comparison of the models with observations. Firstly, to achieve the same 30 GHz intensity, higher local densities are required for spinning nano-silicates than for nano-carbons. To obtain the same intensity as spinning nano-carbons in a medium with $n_{\text{H}} = 5 \text{ H/cm}^3$ at $G_0 = 1$, for ex-

ample, the nano-silicate model requires densities of about 100 to 1000 H/cm^3 . This difference is mainly explained by the difference in the contribution of the IR emission to the rotational excitation of the sub-nanometre grains responsible for the SED of the spinning dust (left panel in Fig. 4). In their Eqs. 95 and 106, Silsbee et al. (2011) indeed showed that the IR excitation and damping rates are proportional to $\int_0^\infty I_\nu/\nu^2 d\nu$ and $\int_0^\infty I_\nu/\nu d\nu$, respectively. Thus, for the case $n_{\text{H}} = 0.1 \text{ H/cm}^3$ and $G_0 = 1$ presented in Fig. 4 (dashed lines), the rotational excitation by IR emission is a factor 0.8 lower and the braking is a factor 1.5 higher for a 0.45 nm nano-silicate than for a nano-carbon of the same size. These discrepancies become even larger with increasing size (factors 0.6 and 7.5, respectively, for 0.6 nm nano-grains), which explains that the SEDs for nano-silicates are narrower than for nano-carbons on the low frequency side (right panel in Fig 4). These differences in the spinning SED intensity and width imply that if the gas distribution in the different interstellar medium phases along a given line of sight is known, it should be possible in principle to determine the types of grains that are the dominant AME carriers. Then, regardless of the gas density used to model the spinning dust emission, the peak frequency and the width of the spectra differ sufficiently between spinning nano-carbons and nano-silicates to result in significantly different $I_{30\text{GHz}}/I_{40\text{GHz}}$ and $I_{30\text{GHz}}/I_{20\text{GHz}}$ intensity ratios (see the example presented in the right panel of Fig. 4). This indicates that several frequencies and not only one (i.e. 30 GHz) are required to characterise AME. Correlating the 30 GHz AME with the 20 and 40 GHz AME is therefore more discriminating

than using the mid- to far-IR emission to characterise the AME carriers.

4. CNM versus WNM fraction in the diffuse neutral interstellar medium

Unlike thermal dust emission, spinning dust emission depends not only on the radiation field, but also on the gas density, as we showed in Sect. 3.3. The local gas properties impact the total intensity of the rotational spectrum, its peak frequency, and its width. This implies that to effectively model the AME and its correlation with other observed quantities, a realistic estimate of the gas density distribution is essential.

The diffuse neutral medium on which we focus can be described as a two-phase medium (e.g. Field et al. 1969; McKee & Ostriker 1977; Wolfire et al. 2003). At thermal equilibrium, the principal heating and cooling processes acting on the interstellar gas allow two thermally stable HI phases that are distinguished by their density and temperature: a cold neutral medium (CNM) with a low kinetic temperature $T \sim 30 - 200$ K and medium density $n_{\text{H}} \sim 5 - 120$ H/cm³, and a warm neutral medium (WNM) with a high temperature $T \sim 4\,100 - 8\,800$ K and low density $n_{\text{H}} \sim 0.03 - 1.3$ H/cm³. These two phases have been confirmed observationally (e.g. Liszt et al. 1993; Heiles & Troland 2003; Nguyen et al. 2019; Murray et al. 2020). However, it has been shown that a significant fraction of the WNM is cooler than expected ($T \sim 500 - 5\,000$ K) and thus falls into the thermally unstable regime. The exact proportion of this unstable HI is still debated (e.g. Heiles & Troland 2003; Murray et al. 2018), however.

Observations show that the CNM fraction, $f_{\text{CNM}} = N_{\text{HI}}^{\text{CNM}} / (N_{\text{HI}}^{\text{CNM}} + N_{\text{HI}}^{\text{WNM}})$, increases with the total column density of HI and in the surroundings of molecular clouds as well (e.g. Stanimirović et al. 2014). For very diffuse high-latitude sightlines, with HI column densities ranging from 3×10^{16} to a few 10^{21} cm², Murray et al. (2015) found that f_{CNM} extends from less than 0.1 to 0.51, with a median value of 0.20. This agrees with the median $f_{\text{CNM}} = 0.23$ measured by Heiles & Troland (2003) for sightlines with $|b| > 10^\circ$ and N_{HI} from a few 10^{20} to a few 10^{21} H/cm². Stanimirović et al. (2014) further showed that for column densities from $\sim 10^{18}$ to a few 10^{21} H/cm², the HI column density of the WNM is relatively uniform, whereas at $N_{\text{HI}} \sim 10^{21}$ H/cm², the CNM fraction increases from almost negligible to $\sim 40\%$ around Perseus, with a median value of 33%. Regions such as Perseus are representative of the areas we selected for our study (Fig. 1), and it is indeed included in the mask defined in Sect. 2.4, as are the Taurus and Gemini regions, for which Nguyen et al. (2019) found $f_{\text{CNM}} = 37\%$ and 16%, respectively. Similar results were found in the California, Rosette, MonOB1, and NGC2264 regions (Nguyen et al. 2019), which are also included in our mask.

Of the sight lines included in our study, 92% have $5 \times 10^{20} \leq N_{\text{HI}} \leq 5 \times 10^{21}$ H/cm² and are above the Galactic Plane. We therefore make the reasonable assumption below that in order to model AME by spinning nano-dust emission, a model is acceptable only if it uses a mixture of CNM and WNM with $0.05 \leq f_{\text{CNM}} \leq 0.4$ and if it matches the AME and mid-IR brightness for HI column densities matching the distribution shown in Fig. 2.

5. Modelling results

To test the different models, we considered CNM/WNM mixtures with $f_{\text{CNM}} = 0$ to 0.5 in steps of 0.05 illuminated by the

Mathis et al. (1983) radiation field with $G_0 = 1$. According to Fanciullo et al. (2015), the typical G_0 variations range from ~ 0.8 to 1.4. The HI column density was set equal to the median, the mean, or the mode of the N_{HI} distribution (see Fig. 2). A model was considered acceptable when inside the contours that encompass 75% of the pixels simultaneously for all three ratios of AME_{30 GHz} versus AME_{20 GHz}, AME_{30 GHz} versus AME_{40 GHz}, and AME_{30 GHz} versus dust emission in the IRAS 12 μm filter for at least one of the tested column densities. All models were run for both nano-carbons and nano-silicates with the properties described in Sect. 3.1. Figures 5 and 6 show the results.

5.1. Digression from observation correlations

Before we describe the details of the modelling, we explored the level of correlation between the different data sets (Fig. 5). Thanks to the new treatment applied to the IRAS data (see Appendix A), which excludes the noisiest areas (see Sect. 2.4), the strength of the linear correlation of the AME for an angular resolution of 1° is as good with the emission at 12 μm as with the emission at 100 μm : the Pearson correlation coefficients are $r_p = 0.96$ and 0.94, respectively. As expected, matter correlates with matter, which shows that our results will not be limited by data problems, but simply by our level of understanding of the dust. Figure 5 shows that the data dispersion remains relatively high, which needs to be explained either by different environments (our mask includes 24% of the sky) or by variations in the nano-grain properties (nature, size distribution, abundance, and electric dipole moment). If suitable matches between the models and the data are not possible, then the spinning nano-grain hypothesis has to be discarded.

5.2. Spinning nano-carbon dust

The model of spinning nano-carbon grains is able to reproduce the observed trends in Fig. 5 (black symbols), but these results do not allow us to constrain the density of the WNM because all of the tested values, $0.05 \leq n_{\text{H}}^{\text{WNM}} \leq 1$ H/cm³, yield solutions for pixels within both the 75% and 50% contours. However, we do note two interesting results. Firstly, the CNM density depends on the WNM density, and a denser WNM implies a denser CNM. For example, for models with a $n_{\text{H}}^{\text{WNM}} = 0.1$ H/cm³, the CNM density must be between 20 and 40 H/cm³. If $n_{\text{H}}^{\text{WNM}} = 0.6$ H/cm³, however, $n_{\text{H}}^{\text{CNM}}$ must be between 30 and 60 H/cm³, and if $n_{\text{H}}^{\text{WNM}} = 1$ H/cm³, then $n_{\text{H}}^{\text{CNM}}$ must be between 40 and 100 H/cm³. Secondly, all viable models require $0.1 \leq f_{\text{CNM}} \leq 0.2$, which is in agreement with the observational studies cited in Sect. 4. This also agrees with the results of Ysard et al. (2010), who used the IRIS map at 12 μm and the 23 GHz AME map derived by Miville-Deschênes et al. (2008) from WMAP data to study 27 regions of a few square degrees, which are all included in our mask. With a spinning PAH model, they obtained $f_{\text{CNM}} \sim 10\%$ for all regions and $m \sim 0.4$ D for most of them. This is a good indication that models using carbonaceous nano-grains give comparable results regardless of their exact nature.

The grain electric dipole moment is probably the most uncertain dust parameter in our modelling. We therefore also show the results for the same nano-carbon dust, but with a higher dipole moment of $m = 0.5$ D (pink symbols in Fig. 5). The results for spinning nano-carbon grains still hold, but the required density of the WNM for the models that fit cannot exceed 0.7 H/cm³. With a higher electric dipole moment, the spectrum of the spin-

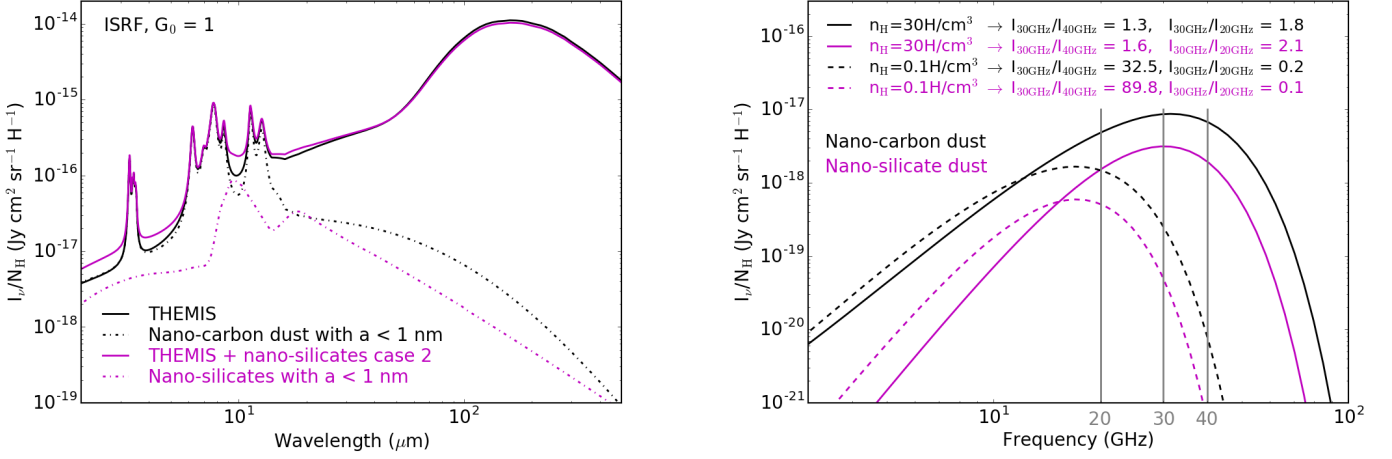


Fig. 4. Comparison of mid-IR to microwave SEDs. Left: SED of thermal dust emission for dust models without (black lines) and with (magenta lines) nano-silicate dust for $G_0 = 1$. In both cases, the dash-dotted lines show the contribution of the smallest nano-grains with $a < 1$ nm that cause the spinning-dust emission. The nano-silicates are those of case 2, which are the closest in size distribution and electric dipole moment to the THEMIS nano-carbon dust. Right: Corresponding spinning-dust emission for media with $n_{\text{H}} = 0.1$ and 30 H/cm^3 as solid and dashed lines, respectively.

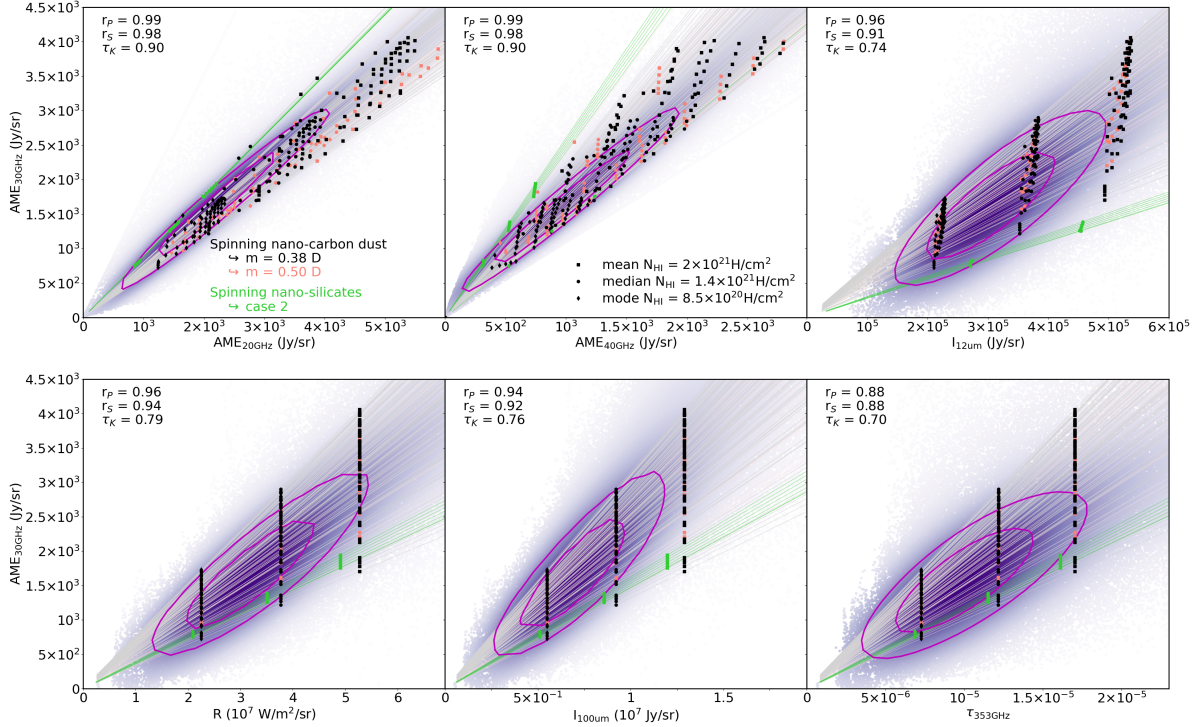


Fig. 5. Comparison of observed and modelled correlations. Top from left to right: observations are plotted as density of points maps of $\text{AME}_{30 \text{ GHz}}$ vs. $\text{AME}_{20 \text{ GHz}}$, vs. $\text{AME}_{40 \text{ GHz}}$, and vs. dust emission in the $12 \mu\text{m}$ IRAS filter. Bottom from left to right: Observations are plotted as density of points maps of $\text{AME}_{30 \text{ GHz}}$ vs. radiance, vs. dust emission in the $100 \mu\text{m}$ IRAS filter, and vs. optical depth at 353 GHz . For all panels, we overplot the contours enclosing 50% of the pixels (internal contour) and 75% of the pixels (external contour). The models fitting the observations are shown with black and pink symbols for spinning nano-carbon dust, $m = 0.38$ and 0.5 D , respectively, and green symbols for spinning nano-silicate dust (case 2; see Sect. 5 for details). Squares, circles, and diamonds show models scaled to the mean ($N_{\text{H}} = 2 \times 10^{21} \text{ H/cm}^2$), the median ($N_{\text{H}} = 1.4 \times 10^{21} \text{ H/cm}^2$), and the mode HI column density ($N_{\text{H}} = 8.5 \times 10^{20} \text{ H/cm}^2$), respectively. The light grey, pink, and green lines show the same models for HI column densities extending over the entire observational range $10^{20} \leq N_{\text{H}} \leq 1.4 \times 10^{22} \text{ H/cm}^2$. The various model points show spinning-dust models for different f_{CNM} values (see Sect. 5.2 for details). The r_P , r_S , and τ_K give the Pearson correlation coefficient, the Spearman rank-order correlation coefficient, and the Kendall's tau, respectively.

ning nano-carbon shifts to the lower frequency side that is dominated by the WNM contribution. To avoid overestimating the intensity at 20 GHz , the rotational excitation by the gas in the WNM must be lower. This requires a lower gas density.

For consistency, we also show the $\text{AME}_{30 \text{ GHz}}$ correlation with radiance (proportional to the radiation field and the column density), the intensity in the IRAS $100 \mu\text{m}$ band (emission from large grains at thermal equilibrium), and the dust opacity at

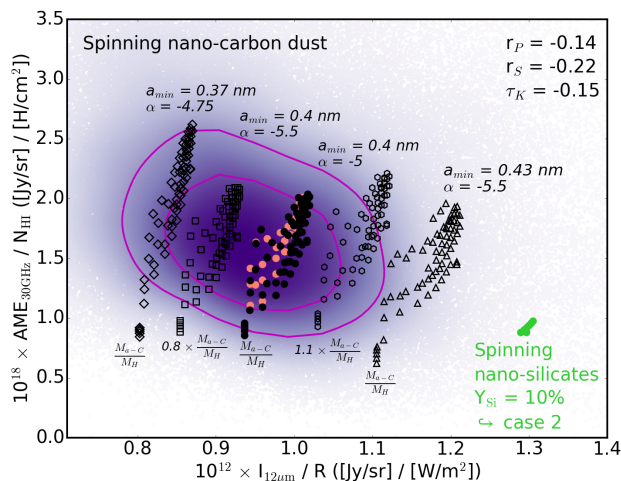


Fig. 6. Density of the points map of $\text{AME}_{30\text{ GHz}}/N_{\text{HI}}$ vs. $I_{12\mu\text{m}}/R$. We overplot the contours enclosing 50% of the pixels (internal contour) and 75% of the pixels (external contour). The r_P , r_S , and τ_K give the corresponding Pearson correlation coefficient, the Spearman rank-order correlation coefficient, and the Kendall's tau, respectively. The same models as in Fig. 5 are shown with black and pink circles for spinning nano-carbon dust, $m = 0.38$ and 0.5 D, respectively, and green circles for spinning nano-silicate dust (case 2), each symbol showing a different value of f_{CNM} (see Sects. 5.2 and 5.3 for details). For spinning nano-carbon dust, we show models with the same f_{CNM} but with variations in the size distribution and dust abundance. The standard THEMIS size distribution with $a_{\text{min}} = 0.4$ nm and $\alpha = -5$, where α is the a-C nano-particle power-law exponent, is shown for $m = 0.38$ D (black circles). We show this same model, but with an abundance increase of 10% (hexagons). The squares show $a_{\text{min}} = 0.4$ nm, $\alpha = -5.5$, and an abundance decrease by 20%. The triangles show $a_{\text{min}} = 0.43$ nm and $\alpha = -5.5$, and the diamonds show $a_{\text{min}} = 0.37$ nm and $\alpha = -4.75$ with the standard model abundances.

353 GHz. All models that are in accordance with the AME and the mid-IR emission also agree with these far-IR/submm emission (derived) observations. This illustrates the consistency of THEMIS at all wavelengths.

Figure 6 shows $\text{AME}_{30\text{ GHz}}/N_{\text{HI}}$ as a function of $I_{12\mu\text{m}}/R$. When we assume that there is no nano-silicate dust in the diffuse interstellar medium, $I_{12\mu\text{m}}/R$ is proportional to the nano-carbon dust abundance. According to Fanciullo et al. (2015), the typical G_0 variations range from ~ 0.8 to 1.4 in the diffuse interstellar medium, which leads to variations in $\text{AME}_{30\text{ GHz}}/N_{\text{HI}}$ of ~ -4 to $+8\%$ for the CNM/WNM mixtures required by the viable spinning-dust models shown in Fig. 5. The models that best account for the observations presented so far also agree with the correlations in the ratios (full black and pink dots in Fig. 6 for $m = 0.38$ and 0.5 D, respectively). If it is indeed due to spinning dust, the $\text{AME}_{30\text{ GHz}}/N_{\text{HI}}$ ratio should be roughly proportional to the nano-carbon dust abundance. There is no obvious correlation in the data with a Pearson correlation coefficient of -0.14 . On the one hand, this might be an illustration of the fact that the excitation of the rotation of nano-grains depends on interactions with the gas and also on the UV radiation field, whereas the mid-IR emission only depends on the latter. On the other hand, the observed dispersion could be the result of small variations in the nano-grain size distribution. The nano-carbon grain dust population, whether PAHs or amorphous hydrocarbons is most strongly affected by stellar photo-processing and shock waves, which both lead to variations in their size distribution and abun-

dance (e.g. Bocchio et al. 2014; Murga et al. 2019; Murga 2020; Joblin et al. 2020; Schirmer et al. 2020). The observed dispersion in the correlations of the ratios can be explained by small variations in the size distribution and abundance (black symbols in Fig. 6). Photo-processing studies show that a decrease in the nano-grain abundance is also associated with a change in the size distribution. For example, Schirmer et al. (2020) showed that in the Horsehead nebula, the slope of the nano-carbon dust size distribution steepens from $n(a) \propto a^{-5}$ to $n(a) \propto a^{-5.5}$ to -7.5 . For the least extreme case, $n(a) \propto a^{-5.5}$ and a 20% decrease in the grain abundance, we obtain the squares in Fig. 6. Our results also show that a slight increase in the nano-carbon dust abundance (hexagons), a small increase in the minimum size coupled to a steeper size distribution slope (triangles), or a shallower size distribution coupled to a smaller minimum size (diamonds) can explain the observed dispersion. The minimum size and slope of the size distribution are indeed degenerate because they both control the quantity of the smallest nano-grains, which cause the AME. These models are also consistent with the correlations presented in Fig. 5.

5.3. Spinning nano-silicate dust

For the spinning nano-silicates with the highest electric dipole moment (cases 3 and 4, $m = 1$ D), it is impossible to simultaneously fit the ratios of $\text{AME}_{30\text{ GHz}}$ versus $\text{AME}_{20\text{ GHz}}$ and $\text{AME}_{30\text{ GHz}}$ versus $\text{AME}_{40\text{ GHz}}$. This electric dipole moment is indeed high enough to significantly slow the rotation speed down and thus leads to spinning emission that peaks at lower frequencies than observed. This implies that even if it is possible to reproduce the intensity level at a single given frequency, for instance at 30 GHz, the spectral shape will be incorrect and accordingly, the required intensities at the two other frequencies cannot be retrieved. We note that the quantum mechanical calculations performed by Macià Escatllar & Bromley (2020) and Mariñoso Guiu et al. (2021) show that Mg-rich nano-silicates will always have $m > 1$ D, even when they are covered by an ice layer. However, high dipole moments like this for nano-silicates appear to be inconsistent with the observations (see also Hoang et al. 2016; Hensley & Draine 2017).

Only nano-silicates with a lower dipole moment and a size distribution centred on the smallest grains result in a spinning emission within the 75% contour (case 2: $m = 0.3$ D and $\sigma = 0.1$, green symbols in Fig. 5). However, this works for only six CNM/WNM mixtures, all having $f_{\text{CNM}} = 0.3$ and a CNM density $n_{\text{H}} = 20$ H/cm³, with the WNM density varying from 0.5 to 1 H/cm³. Only so few models fall within the 75% contour because the intensity in the IRAS $12\mu\text{m}$ band is too high. This is more obvious when we plot the $\text{AME}_{30\text{ GHz}}/N_{\text{HI}}$ ratio over $I_{12\mu\text{m}}/R$, for which the nano-silicates are within the observed dispersion, but not within the 75% contour (green dots in Fig. 6). This leads us to the following conclusion: if $Y_{\text{Si}} = 10\%$, then nano-silicates can only marginally contribute to the AME, regardless of their properties.

The only way to reduce the nano-silicate mid-IR emission is to decrease Y_{Si} . However, for $G_0 = 1$, the nano-silicates only account for about 18% of the total intensity because the IRAS $12\mu\text{m}$ filter is very wide ($\sim 7\mu\text{m}$). They do, however, account for 45% of the total intensity at the peak frequency of the relatively narrow silicate spectral feature at $9.8\mu\text{m}$. As a result, halving Y_{Si} , only decreases $I_{12\mu\text{m}}$ by about 9%, while the 30 GHz spinning emission is decreased by 50%. We therefore come to the same conclusion, that nano-silicates can, at best, only contribute marginally to the observed AME.

Hensley & Draine (2017) suggested that uncertainties in the grain equilibrium charge distribution could lead to an uncertainty in the nano-silicate spinning SED, in particular if the number of negatively charged grains is underestimated. These are indeed more rotationally excited. As discussed in Weingartner & Draine (2001), the grain charge distribution and the number of negatively charged grains depends on the bulk work function W , which we take to be 4.97 eV for silicates, following Kimura (2016, and references therein) instead of 8 eV, which is the standard value often adopted for all grains, whether they are based on carbon or silicate (Draine 1978). To test the influence of this choice, we ran calculations with $W = 8$ eV. The same fitting procedure changes our results very little: only case 2 nano-silicates give a few models within the 75% contour for the same CNM and WNM gas densities. The only difference is that f_{CNM} is decreased to 0.25. This is a consequence of the fact that negatively charged grains are not abundant in diffuse gas that is pervaded by UV.

Our conclusions might be biased because THEMIS comprises amorphous aromatic-rich nano-carbon grains rather than so-called ‘astro-PAHs’. This is not the case. For the PAHs of the Compiègne et al. (2011) model, the difference in the IRAS 12 μm band is only $\sim 3\%$ in favour of THEMIS. The difference might come from the adopted silicate optical properties, but this is again not the case. When we compare the Draine & Li (2007) model, which contains both PAHs and nano-silicates in more or less the same proportions as our case 2, at $G_0 = 1$, the difference in the IRAS 12 μm band is $\sim 5\%$, which is again in favour of THEMIS. This means that for the diffuse interstellar medium sky area (Fig. 1) we considered, all models that attempt to explain the AME, at several frequencies, with nano-silicates alone have the same problem, whether they use PAHs or amorphous nano-carbon grains. Hoang et al. (2016) did not have this problem because they did not consider the mid-IR emission. They tested their model against the UV extinction, polarisation of starlight, and the polarisation of the AME. They were able to place constraints on both $Y_{\text{Si}} \leq 10\%$ and $m \geq 0.4$ D (see their Fig. 8). With regard to the results of Hensley et al. (2016), $4 \leq Y_{\text{Si}} \leq 15\%$ and $0.3 \leq m \leq 1$ D, the difference can probably be reduced to a single aspect: the normalisation of their spectra. Their mid-IR spectrum is that of the translucent cloud DCld 300.2-16.9. According to Ingalls et al. (2011, and references therein), DCld 300.2-16.9 is a CNM cloud that is illuminated by the ISRF with $G_0 = 1$, with a column density of $\sim 4 \times 10^{21}$ H/cm², that was affected by supernova explosions from the Sco-Cen OB association about $(2-6) \times 10^5$ years ago. This spectrum was scaled to the HI-correlated dust emission in the DIRBE bands as in Dwek et al. (1997): $I_{12\mu\text{m}} = 3.16 \times 10^{-16}$ Jy cm²/sr/H and was then associated with the median AME Planck COMMANDER spectrum normalised to 3×10^{-18} Jy cm²/sr/H at 30 GHz. This is far from the bulk of the pixels of the intermediate-latitude regions that we studied here.

5.4. Combined nano-carbon and nano-silicate dust emission

If nano-carbon and nano-silicate dust co-exist in the diffuse interstellar medium, it is reasonable to assume that both will produce spinning dust emission. For carbonaceous nano-dust, we have clear and abundant observational evidence for their existence in non-negligible quantities in the interstellar medium, while the case is not so clear-cut for nano-silicates. In order to be comprehensive, we therefore repeated the fitting procedure with the assumption that both populations contribute to the AME. We did this for several values of Y_{Si} ($= 10, 5$ and 1%) for case 2

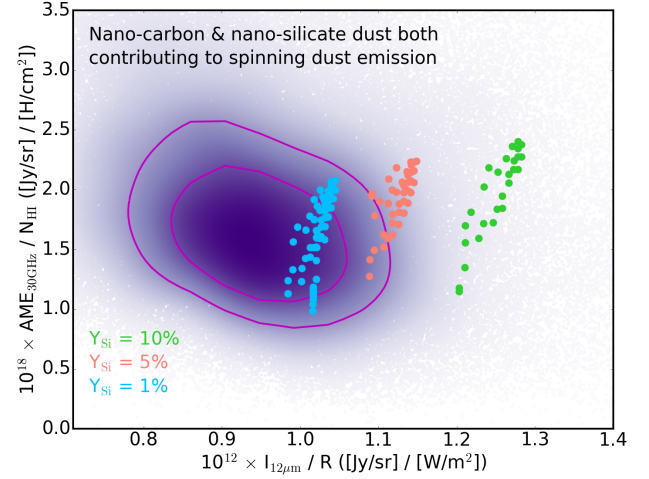


Fig. 7. $\text{AME}_{30\text{ GHz}}/N_{\text{HI}}$ vs. $I_{12\mu\text{m}}/R$ as in Fig. 6. The green dots show best fitting models in which both the nano-carbon dust and the nano-silicate dust produce spinning emission (case 2, $Y_{\text{Si}} = 10\%$, $m = 0.3$ D, $\sigma = 0.1$), with each point showing a different f_{CNM} value. Model calculations for lower abundances of nano-silicates are shown: $Y_{\text{Si}} = 5\%$ (pink dots) and $Y_{\text{Si}} = 1\%$ (blue dots).

nano-silicates ($m = 0.3$ D and $\sigma = 0.1$). All of these nano-silicate abundances led to acceptable CNM/WNM mixtures, and we show the corresponding model results in Fig. 7. The default value $Y_{\text{Si}} = 10\%$ is within the dispersion, but does not fall within the contours surrounding the bulk of the pixels. If the abundance of nano-silicates is halved, then the models are at the edge of the 75% contour. When the abundance is further lowered to $Y_{\text{Si}} = 1\%$, the models fall within the 50% contour, but remain on the high $I_{12\mu\text{m}}/R$ side, and nano-silicates account only for 3 - 5% of the AME at 30 GHz, depending on the CNM/WNM mixture. We do not show cases 1, 3, and 4 because the discrepancy comes mainly from the $I_{12\mu\text{m}}/R$ ratio. Cases 2 and 4 have the exact same $I_{12\mu\text{m}}/R$, which does not depend on m , but just on σ . Cases 1 and 3 are similar and have the same radiance (no changes in the larger grain populations), and the $I_{12\mu\text{m}}$ values vary by no more than 2% when compared to cases 2 and 4.

Fig. 7 indicates that (1) if both nano-grain populations co-exist in the diffuse interstellar medium, then the AME must come predominantly from nano-carbon dust emission, and (2) if both populations have non-zero permanent electric dipole moments, then the abundance of nano-silicates cannot exceed $\sim 1\%$. This upper limit agrees with the findings of Désert et al. (1986), Macià Escatllar & Bromley (2020), and Mariñoso Guiu et al. (2021). All three studies derive an upper limit of $Y_{\text{Si}} = 1\%$. This is lower than the upper limit of $\sim 10\%$ reported by Li & Draine (2001). The difference most probably comes from the line of sight chosen by Li & Draine (2001) to test their model ($l = 44^\circ 20'$, $b = -0^\circ 20'$), which is in the Galactic Plane and has a relatively high column density ($N_{\text{H}} = 4.3 \times 10^{22}$ H/cm²) and a radiation field with $G_0 = 2$. This line of sight is therefore not representative of the bulk of the diffuse interstellar medium lines of sight at intermediate latitudes.

6. Conclusion

Using The Heterogeneous dust Evolution Model for Interstellar Solids (THEMIS, Jones et al. 2017), we investigated whether the nature of the grains at the origin of the AME measured by

the Planck Collaboration (Planck Collaboration et al. 2016b) in the Galactic diffuse interstellar medium can be identified. Model grids were created with the DustEM numerical tool (Compiègne et al. 2011) and were compared with observations and parameters derived from them, from the mid-IR to the microwave. Our results are listed below.

First, nano-carbon dust can explain all the observations for medium properties, in agreement with the latest findings about the separation of CNM and WNM in the diffuse interstellar medium. The dispersion in the observations can be accounted for with little variations in the dust size distribution, abundance, or electric dipole moment. Second, regardless of the properties and the abundance of the nano-silicate dust considered, spinning nano-silicates are formally excluded as the sole source of the AME. Third, the best agreement with observations is obtained when the emission of spinning nano-carbons alone is taken into account. The addition of a nano-silicate component takes the model beyond the maximum density area of the correlation plots. However, a marginal participation of these nano-silicates to the AME production cannot be excluded as long as their abundance does not exceed $Y_{\text{Si}} \sim 1\%$.

Our results reconcile large- and small-scale studies. Careful investigations of the carrier nature and evolution through modelling and data correlations, have linked AME and spinning nano-carbonaceous dust in these studies, be they amorphous hydrocarbons or PAHs. The AME is thus very promising for tracing the evolution of carbonaceous grains because the spinning emission does not only depend on the grain properties, but also on the properties of the immediate local medium. This should allow testing the models of grain evolution in a strongly constraining way, whether they are due to UV photons or shocks.

Acknowledgements. We thank our anonymous referee whose careful reading and interesting comments helped to clarify and improve the paper. This work was supported by the Programme National PCMI of CNRS/INSU with INC/INP co-funded by CEA and CNES. Finally, thanks to Dan Pineau who helped me fix my office chair, an essential tool if ever there was one.

References

- Abergel, A., Boulanger, F., Delouis, J. M., Dudziak, G., & Steindling, S. 1996, *A&A*, 309, 245
- Ali-Haïmoud, Y., Hirata, C. M., & Dickinson, C. 2009, *MNRAS*, 395, 1055
- AMI Consortium: Scaife, A. M. M., Green, D. A., Pooley, G. G., et al. 2010, *MNRAS*, 403, L46
- Arab, H., Abergel, A., Habart, E., et al. 2012, *A&A*, 541, A19
- Bell, A. C., Onaka, T., Galliano, F., et al. 2019, *PASJ*, 71, 123
- Bennett, C. L., Larson, D., Weiland, J. L., et al. 2013, *ApJS*, 208, 20
- Bernard, J. P., Abergel, A., Ristorcelli, I., et al. 1999, *A&A*, 347, 640
- Berné, O., Joblin, C., Deville, Y., et al. 2007, *A&A*, 469, 575
- Bocchio, M., Jones, A. P., & Slavin, J. D. 2014, *A&A*, 570, A32
- Campeggio, L., Strafella, F., Maiolo, B., Elia, D., & Aiello, S. 2007, *ApJ*, 668, 316
- Casassus, S., Dickinson, C., Cleary, K., et al. 2008, *MNRAS*, 391, 1075
- Casassus, S., Vidal, M., Arce-Tord, C., et al. 2021, *MNRAS*, 502, 589
- Cepeda-Arroita, R., Harper, S. E., Dickinson, C., et al. 2021, *MNRAS*, 503, 2927
- Compiègne, M., Abergel, A., Verstraete, L., & Habart, E. 2008, *A&A*, 491, 797
- Compiègne, M., Verstraete, L., Jones, A., et al. 2011, *A&A*, 525, A103
- Désert, F. X., Boulanger, F., Leger, A., Puget, J. L., & Sellgren, K. 1986, *A&A*, 159, 328
- Dickinson, C., Ali-Haïmoud, Y., Barr, A., et al. 2018, *New A Rev.*, 80, 1
- Draine, B. T. 1978, *ApJS*, 36, 595
- Draine, B. T. & Hensley, B. 2013, *ApJ*, 765, 159
- Draine, B. T. & Lazarian, A. 1998a, *ApJ*, 508, 157
- Draine, B. T. & Lazarian, A. 1998b, *ApJ*, 508, 157
- Draine, B. T. & Lazarian, A. 1999, *ApJ*, 512, 740
- Draine, B. T. & Li, A. 2007, *ApJ*, 657, 810
- Dwek, E., Arendt, R. G., Fixsen, D. J., et al. 1997, *ApJ*, 475, 565
- Fanciullo, L., Guillet, V., Aniano, G., et al. 2015, *A&A*, 580, A136
- Fanciullo, L., Guillet, V., Boulanger, F., & Jones, A. P. 2017, *A&A*, 602, A7
- Ferland, G. J., Korista, K. T., Verner, D. A., et al. 1998, *PASP*, 110, 761
- Field, G. B., Goldsmith, D. W., & Habing, H. J. 1969, *ApJ*, 155, L149
- Flagey, N., Noriega-Crespo, A., Boulanger, F., et al. 2009, *ApJ*, 701, 1450
- Górski, K. M., Hivon, E., Banday, A. J., et al. 2005, *ApJ*, 622, 759
- Guhathakurta, P. & Draine, B. T. 1989, *ApJ*, 345, 230
- Harper, S. E., Dickinson, C., & Cleary, K. 2015, *MNRAS*, 453, 3375
- Haslam, C. G. T., Salter, C. J., Stoffel, H., & Wilson, W. E. 1982, *A&AS*, 47, 1
- Heiles, C. & Troland, T. H. 2003, *ApJ*, 586, 1067
- Hensley, B. S. & Draine, B. T. 2017, *ApJ*, 836, 179
- Hensley, B. S., Draine, B. T., & Meisner, A. M. 2016, *ApJ*, 827, 45
- HIPI Collaboration, Ben Bekhti, N., Flöer, L., et al. 2016, *A&A*, 594, A116
- Hoang, T. & Lazarian, A. 2016, *ApJ*, 821, 91
- Hoang, T., Vinh, N.-A., & Quynh Lan, N. 2016, *ApJ*, 824, 18
- Ingalls, J. G., Bania, T. M., Boulanger, F., et al. 2011, *ApJ*, 743, 174
- Joblin, C., Wenzel, G., Rodríguez Castillo, S., et al. 2020, in *Journal of Physics Conference Series*, Vol. 1412, *Journal of Physics Conference Series*, 062002
- Jones, A. P. 2009, *A&A*, 506, 797
- Jones, A. P. 2012a, *A&A*, 540, A1
- Jones, A. P. 2012b, *A&A*, 540, A2
- Jones, A. P. 2012c, *A&A*, 542, A98
- Jones, A. P., Fanciullo, L., Köhler, M., et al. 2013, *A&A*, 558, A62
- Jones, A. P., Köhler, M., Ysard, N., Bocchio, M., & Verstraete, L. 2017, *A&A*, 602, A46
- Jones, A. P., Ysard, N., Köhler, M., et al. 2014, *Faraday Discussions*, 168, 313
- Juvela, M., Neha, S., Mannfors, E., et al. 2020, *A&A*, 643, A132
- Kelsall, T., Weiland, J. L., Franz, B. A., et al. 1998, *ApJ*, 508, 44
- Kim, S.-H., Martin, P. G., & Hendry, P. D. 1994, *ApJ*, 422, 164
- Kimura, H. 2016, *MNRAS*, 459, 2751
- Kogut, A., Banday, A. J., Bennett, C. L., et al. 1996, *ApJ*, 460, 1
- Köhler, M., Stepnik, B., Jones, A. P., et al. 2012, *A&A*, 548, A61
- Köhler, M., Ysard, N., & Jones, A. P. 2015, *A&A*, 579, A15
- Laureijs, R. J., Clark, F. O., & Prusti, T. 1991, *ApJ*, 372, 185
- Lefèvre, C., Pagani, L., Juvela, M., et al. 2014, *A&A*, 572, A20
- Leitch, E. M., Readhead, A. C. S., Pearson, T. J., & Myers, S. T. 1997, *ApJ*, 486, L23
- Li, A. & Draine, B. T. 2001, *ApJ*, 550, L213
- Liszt, H. S., Braun, R., & Greisen, E. W. 1993, *AJ*, 106, 2349
- Macià Escatllar, A. & Bromley, S. T. 2020, *A&A*, 634, A77
- Mariño Guiu, J., Ferrero, S., Macià Escatllar, A., Rimola, A., & Bromley, S. T. 2021, *Frontiers in Astronomy and Space Sciences*, 8, 80
- Mathis, J. S., Mezger, P. G., & Panagia, N. 1983, *A&A*, 128, 212
- Mathis, J. S. & Whiffen, G. 1989, *ApJ*, 341, 808
- McKee, C. F. & Ostriker, J. P. 1977, *ApJ*, 218, 148
- Miville-Deschênes, M.-A. & Lagache, G. 2005, *ApJS*, 157, 302
- Miville-Deschênes, M. A., Ysard, N., Lavabre, A., et al. 2008, *A&A*, 490, 1093
- Murga, M. S. 2020, *INASAN Science Reports*, 5, 298
- Murga, M. S., Khoperskov, S. A., & Wiebe, D. S. 2016, *Astronomy Reports*, 60, 669
- Murga, M. S., Wiebe, D. S., Sivkova, E. E., & Akimkin, V. V. 2019, *MNRAS*, 488, 965
- Murray, C. E., Peek, J. E. G., & Kim, C.-G. 2020, *ApJ*, 899, 15
- Murray, C. E., Stanimirović, S., Goss, W. M., et al. 2015, *ApJ*, 804, 89
- Murray, C. E., Stanimirović, S., Goss, W. M., et al. 2018, *ApJS*, 238, 14
- Nashimoto, M., Hattori, M., Poidevin, F., & Génova-Santos, R. 2020, *ApJ*, 900, L40
- Nguyen, H., Dawson, J. R., Lee, M.-Y., et al. 2019, *ApJ*, 880, 141
- Ormel, C. W., Paszun, D., Dominik, C., & Tielens, A. G. G. M. 2009, *A&A*, 502, 845
- Pilleri, P., Montillaud, J., Berné, O., & Joblin, C. 2012, *A&A*, 542, A69
- Pilleri, P., Reisenfeld, D. B., Zurbuchen, T. H., et al. 2015, *ApJ*, 812, 1
- Planck Collaboration, Abergel, A., Ade, P. A. R., et al. 2014a, *A&A*, 571, A11
- Planck Collaboration, Adam, R., Ade, P. A. R., et al. 2016a, *A&A*, 594, A1
- Planck Collaboration, Adam, R., Ade, P. A. R., et al. 2016b, *A&A*, 594, A10
- Planck Collaboration, Ade, P. A. R., Aghanim, N., et al. 2016c, *A&A*, 594, A25
- Planck Collaboration, Ade, P. A. R., Aghanim, N., et al. 2014b, *A&A*, 565, A103
- Ridderstad, M., Juvela, M., Lehtinen, K., Lemke, D., & Liljeström, T. 2006, *A&A*, 451, 961
- Saajasto, M., Juvela, M., Lefèvre, C., Pagani, L., & Ysard, N. 2021, *A&A*, 647, A109
- Schirmer, T., Abergel, A., Verstraete, L., et al. 2020, *A&A*, 639, A144
- Schlegel, D. J., Finkbeiner, D. P., & Davis, M. 1998, *ApJ*, 500, 525
- Silsbee, K., Ali-Haïmoud, Y., & Hirata, C. M. 2011, *MNRAS*, 411, 2750
- Stanimirović, S., Murray, C. E., Lee, M.-Y., Heiles, C., & Miller, J. 2014, *ApJ*, 793, 132
- Stepnik, B., Abergel, A., Bernard, J. P., et al. 2003, *A&A*, 398, 551
- Tibbs, C. T., Flagey, N., Paladini, R., et al. 2011, *MNRAS*, 418, 1889
- Tibbs, C. T., Watson, R. A., Dickinson, C., et al. 2010, *MNRAS*, 402, 1969
- Vaillancourt, J. E., Andersson, B. G., Clemens, D. P., et al. 2020, *ApJ*, 905, 157
- Vidal, M., Dickinson, C., Harper, S. E., Casassus, S., & Witt, A. N. 2020, *MNRAS*, 495, 1122
- Weingartner, J. C. & Draine, B. T. 2001, *ApJS*, 134, 263
- Wheelock, S., Gautier, T. N., Chillemi, J., et al. 1993, *ISSA Explanatory Supplement*, Tech. rep., Page:
- Wheelock, S. L., Gautier, T. N., Chillemi, J., et al. 1994, *IRAS sky survey atlas: Explanatory supplement*, NASA STI/Recon Technical Report N
- Wolfe, M. G., McKee, C. F., Hollenbach, D., & Tielens, A. G. G. M. 2003, *ApJ*, 587, 278
- Ysard, N., Abergel, A., Ristorcelli, I., et al. 2013, *A&A*, 559, A133
- Ysard, N., Juvela, M., & Verstraete, L. 2011, *A&A*, 535, A89
- Ysard, N., Köhler, M., Jones, A., et al. 2016, *A&A*, 588, A44
- Ysard, N., Köhler, M., Jones, A., et al. 2015, *A&A*, 577, A110
- Ysard, N., Miville-Deschênes, M. A., & Verstraete, L. 2010, *A&A*, 509, L1
- Ysard, N. & Verstraete, L. 2010, *A&A*, 509, A12

Appendix A: Removal of zodiacal residuals at 12 μm

The IRIS maps (Miville-Deschênes & Lagache 2005) were partially corrected for residual zodiacal emission compared to the original IRAS products (ISSA plates – Wheelock et al. 1993). This was achieved by setting the emission at scales larger than 1° to the one of DIRBE, which benefited from a better zodiacal subtraction (Kelsall et al. 1998). Nevertheless, the DIRBE and IRIS maps still show significant zodiacal residuals, especially at 12 and 25 μm (see Fig. A.1). Most of the zodiacal residuals are oriented parallel to the ecliptic plane, but because of the scanning strategy of IRAS, which followed the ecliptic plane, and because of the way zero levels were estimated in the ISSA plates products, there are also residuals perpendicular to the ecliptic plane.

In order to improve on the zodiacal residual subtraction in the IRIS 12 μm band, we performed an adaptive filtering tailored to extracting residual emission oriented along or perpendicular to the ecliptic plane. The full method will be described in a forthcoming paper (Miville-Deschênes et al., in prep). Here we only summarise the processing steps.

The main difficulty in estimating zodiacal residuals based on the map itself (and not returning to the original data timeline) is to separate it from the interstellar medium emission itself, which dominates the signal almost everywhere. To estimate the zodiacal map $Z(\mathbf{r})$ of an emission map $I(\mathbf{r})$ (here the IRIS 12 μm map), we performed a filtering F of a residual map $R(\mathbf{r})$,

$$Z(\mathbf{r}) = F(R(\mathbf{r})),$$

where R is a difference map between the original map I and a reference map I_0 (assumed to be free of zodiacal residuals) times a spatially varying correlation coefficient α ,

$$R(\mathbf{r}) = I(\mathbf{r}) - \alpha(\mathbf{r})I_0(\mathbf{r}).$$

Here the reference map we used is the 100 μm map, which combines the original IRIS map with the map of Schlegel et al. (1998), which has fewer zodiacal residuals at large scales. This was also used in the all-sky dust model of Planck Collaboration et al. (2014a). It is available in the Planck archive⁶.

The correlation coefficient $\alpha(\mathbf{r})$ was estimated benefiting from the healpix gridding of the data. Specifically, α was estimated on a coarser healpix grid (we used $n_{\text{side}} = 32$), where for each large healpix pixel, the linear regression correlation coefficient was calculated using $n_{\text{side}} = 2048$ pixels of I versus I_0 encapsulated in the $n_{\text{side}} = 32$ large pixels. This coarse map of α was then regridded to $n_{\text{side}} = 2048$ to calculate $R(\mathbf{r})$.

The filtering F applied on R was tailored to extract large-scale structures parallel and perpendicular to the ecliptic plane. To do this, we filtered R using a median filtering technique with an elongated window. First a window parallel to the ecliptic plane was used with a width of 20° in ecliptic longitude and only $3'$ in latitude (basically only two pixels). The map of Z we derived in this way was removed from I , and the whole process was reproduced using a perpendicular filtering window of $3'$ in longitude and 40° in latitude.

The resulting 12 μm map obtained after this process is shown in the right panel of Fig. A.1. Faint zodiacal residuals are still visible, but the improvement is significant. It can be evaluated by considering the correlation of the 12 μm emission with other

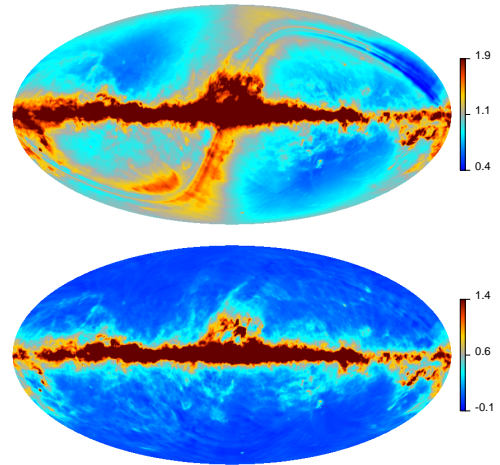


Fig. A.1. All-sky IRIS 12 μm map in MJy/sr. Top: From the IRIS reprocessing (Miville-Deschênes & Lagache 2005). Bottom: After removing the zodiacal residuals.

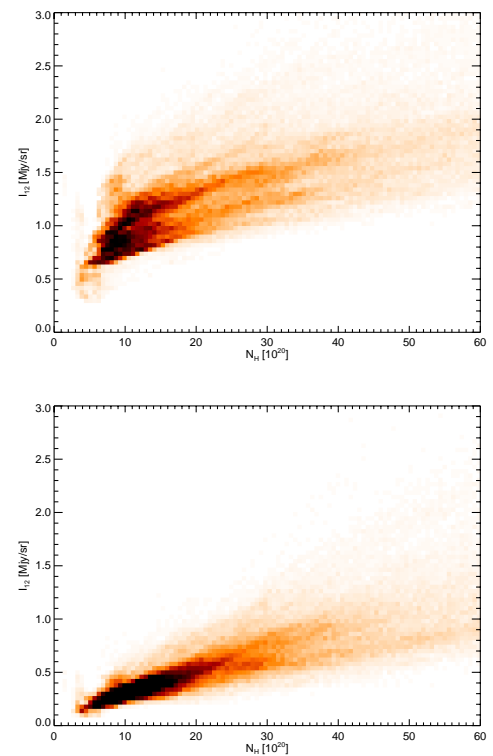


Fig. A.2. Two-dimensional histogram of the 12 μm emission as a function of N_{H} deduced from the $\tau_{353 \text{ GHz}}$ dust optical depth map of Planck Collaboration et al. (2014a) before (top) and after (bottom) zodiacal correction. The data are from the maps used in the current paper; all maps are at 1° resolution, and only the pixels in the mask shown in Fig. 1 were used to build the histograms.

tracers of the interstellar medium column density. As an example, we present in Fig. A.2 the correlation of the original (top) and zodi-corrected (bottom) IRIS 12 μm maps with $\tau_{353 \text{ GHz}}$ (here converted into column density N_{H} Planck Collaboration et al. 2014a), convolved at a resolution of 1° and limited to the pixels we used in our analysis (see the mask shown in Fig. 1). The correlation coefficient is increased from 0.82 to 0.86.

⁶ http://pla.esac.esa.int/pla/aio/product-action?MAP_ID=IRIS_combined_SFD_really_nohole_4_2048.fits